



# Atomic-scale *quasi in-situ* TEM observation on the redistribution of alloying element Cu in a B<sub>4</sub>C/Al composite at the initial stage of corrosion

Y.T. Zhou<sup>a,\*</sup>, Y.N. Zan<sup>a</sup>, Q.Z. Wang<sup>b</sup>, B.L. Xiao<sup>a</sup>, Z.Y. Ma<sup>a,\*</sup>, X.L. Ma<sup>a</sup>

<sup>a</sup>Shenyang National Laboratory for Materials Science, Institute of Metal Research, Chinese Academy of Sciences, 72 Wenhua Road, Shenyang, 110016, China

<sup>b</sup>CAS Key Laboratory of Nuclear Materials and Safety Assessment, Institute of Metal Research, Chinese Academy of Sciences, 72 Wenhua Road, Shenyang, 110016, China

## ARTICLE INFO

### Keywords:

- A. Metal matrix composites
- A. Aluminium
- B. TEM
- C. De-alloying
- C. Pitting corrosion
- C. Segregation

## ABSTRACT

The present study reports an atomic level *quasi in-situ* TEM observation of the redistribution of alloying element Cu in the corrosion process of a B<sub>4</sub>C-reinforced Al-Mg-Si-Cu composite. Cu atoms were found to combine with Mg and form a thin layer at the interfaces between the aluminum matrix and nano-reinforcements (i.e. Mg(Al)B<sub>2</sub> and Al<sub>3</sub>BC). Dealloying of the Cu/Mg-rich layer was revealed. The following decomposition of Mg(Al)B<sub>2</sub> resulted in narrow corrosion trenches forming around Mg(Al)B<sub>2</sub> and then the localized pitting of the matrix. In addition, the liberated Cu ions were then redeposited and formed noble Cu nano-particles upon cathodic Mg(Al)B<sub>2</sub> and B<sub>4</sub>C particles.

## 1. Introduction

B<sub>4</sub>C particles-reinforced aluminum matrix composite (AMC) receives considerable engineering interest these years owing to its neutron absorption capability [1–4]. The composite is used to fabricate the storage and transportation containers for spent nuclear fuels in nuclear industry worldwide. In the solution environment where the fuel is stored, the corrosion resistance of the composite should be seriously evaluated.

As usual, galvanic corrosion is one of the most important considerations when a conducting or semiconducting secondary phase is electrically contacted with the alloy matrix. Therefore, most of the investigations on the corrosion of AMCs were trying to identify the galvanic coupling between the strengthening phases and the matrix [5–11]. Due to the noble corrosion potential of B<sub>4</sub>C particles, they can generate galvanic coupling with the aluminum matrix and serve as cathodic sites. The corrosion rate of B<sub>4</sub>C/Al composite is enhanced with increasing B<sub>4</sub>C contents [11,12]. The galvanic corrosion is also present between the matrix and other strengthening phases. In order to enhance the mechanical properties, some nano-sized strengthening particles are co-introduced into B<sub>4</sub>C/Al composite [13,14]. It was demonstrated that the in-situ formed Mg(Al)B<sub>2</sub> reinforcement in the aluminum matrix acted as cathode and deteriorated the corrosion resistance of the composite [15].

Besides the externally introduced reinforcements, element alloying with the aim of forming a high density of precipitates by ageing is a

very general approach to strengthen the AMCs. There have been a large number of studies on the correlations between heat treatment and corrosion susceptibility of commercially available Al alloys [16]. Instead of forming homogeneously distributed precipitations in the metal matrix, alloying elements are also inclined to segregate at interfaces, e.g. grain boundaries and interphase boundaries. When the AMCs are quenched from high temperatures, the supersaturated vacancies may leave in the grain interior. In the following heat treatment, the vacancy-solute atom complexes tend to be absorbed by the interfaces, leading to the solute segregation at these places [17,18]. Compared with the electrochemical roles played by the secondary phases, the behavior of the solute element segregation was much less studied and consequently far from known. A typical example is the alloying element Cu in B<sub>4</sub>C-reinforced Al-Mg-Si (6xxx series) composite.

In 6xxx series alloys, Cu is commonly present and beneficial to improve the peak hardness and the thermal stability of the alloys by forming Cu-containing precipitates (Q-series) [19–21]. In terms of the corrosion resistance, Cu addition could reduce the metastable pitting events compared to the Cu-free alloys in the same ageing condition due to the replacement of Mg<sub>2</sub>Si phase by Q precipitates [22]. Nevertheless, the Cu addition was demonstrated to increase the intergranular corrosion (IGC) susceptibility of the underaged alloys. The IGC is closely related to the continuous Cu layer and precipitate-free zone at the GBs [23,24]. In B<sub>4</sub>C/Al composite, the B<sub>4</sub>C particles are very reactive with the molten alloy matrix. The reaction products in B<sub>4</sub>C/Al-Mg-Si system, i.e. Al<sub>3</sub>BC and Mg(Al)B<sub>2</sub>, are beneficial to the mechanical properties of

\* Corresponding authors.

E-mail addresses: [ytzhou@imr.ac.cn](mailto:ytzhou@imr.ac.cn) (Y.T. Zhou), [zym@imr.ac.cn](mailto:zym@imr.ac.cn) (Z.Y. Ma).

<https://doi.org/10.1016/j.corsci.2020.108808>

Received 6 December 2019; Received in revised form 27 April 2020; Accepted 8 June 2020

Available online 10 June 2020

0010-938X/ © 2020 Elsevier Ltd. All rights reserved.

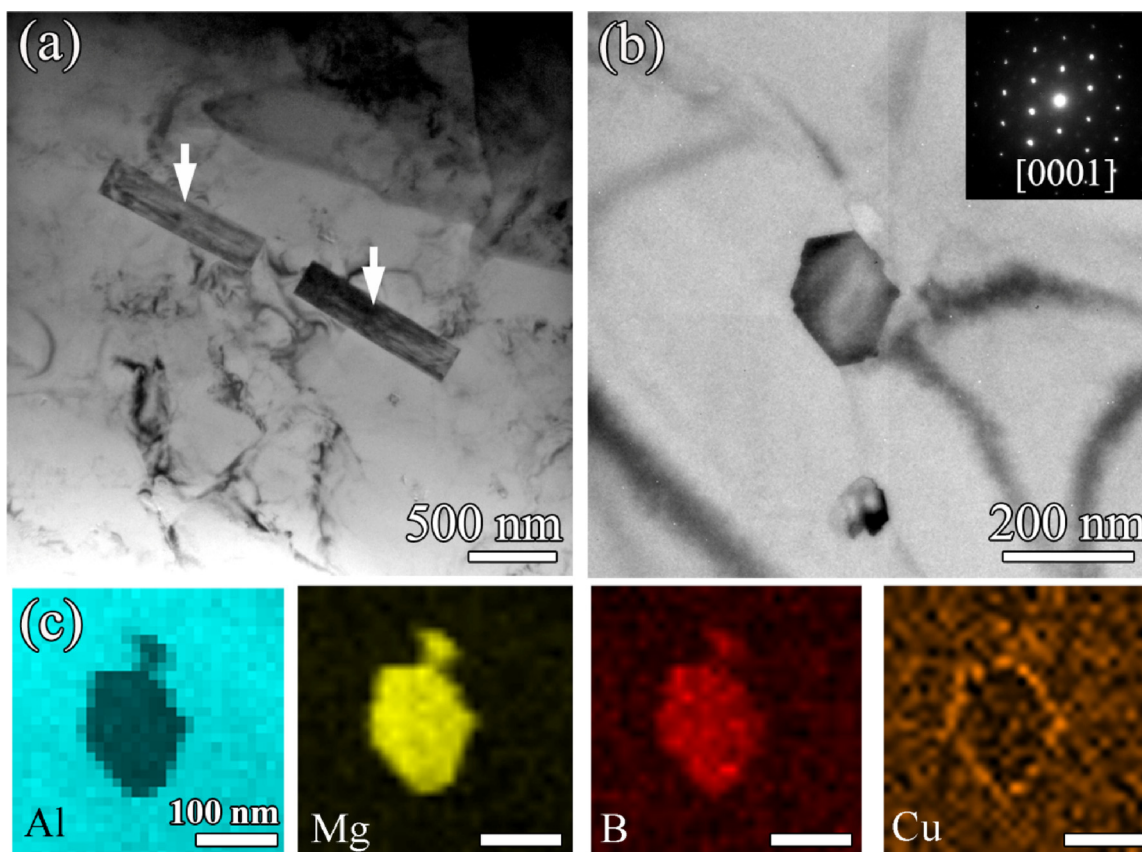


**Fig. 1.** (a) Bright-field TEM image of the  $\text{Mg}(\text{Al})\text{B}_2$  dispersoids in the alloy matrix. (b) Bright-field TEM image and corresponding SAED pattern of a  $\text{Mg}(\text{Al})\text{B}_2$  crystalline along its  $[0001]$  zone-axis. (c) EDS elemental mapping of the  $\text{Mg}(\text{Al})\text{B}_2$  in (b). A thin Cu-rich layer is seen around the particle. (For interpretation of the references to color in this figure legend, the reader is referred to the web version of this article.).

the composite. Owing to the consumption of element Mg, alloying Cu did not form Q-phase but segregated surrounding the  $\text{Al}_3\text{BC}$  and  $\text{Mg}(\text{Al})\text{B}_2$  compounds [25]. Apparently, the effect that Cu played in the corrosion process of the composite could not be interpreted by the knowledge obtained from Cu-containing 6xxx Al alloys.

To understand this issue, proper characterization techniques and methodology are needed. Firstly, in the past decades, the development of aberration correctors made TEM possess sub-Ångstrom resolution and a feasible technique to conduct atomic-scale characterization. In particular, the high-angle annular-dark-field (HAADF) scanning transmission electron microscopy (STEM) mode provides a more applicable choice to direct image heavy solute atoms in alloy matrix (for example, Cu in Al matrix), since the contrast intensity in such mode is proportional to  $Z^{1.7-1.9}$  ( $Z$  is the atomic number) [26]. Secondly, a methodology named *quasi in-situ* TEM investigation which can trace the structural/chemical evolution in the corrosion process by viewing the same location before and after repeated exposure of the TEM specimen in corrosive environment should be promising for this investigation [27–30].

In this work, the very beginning corrosion stage of a  $\text{B}_4\text{C}/\text{Al}-\text{Mg}-\text{Si}-\text{Cu}$  composite associated with the segregated Cu at interphase boundaries were studied using *quasi in-situ* TEM observations under the aberration-corrected TEM platform. The result should be beneficial to interpret the electrochemical/chemical roles of alloying Cu in the composite. Moreover, since solute segregation is popular in aluminum based alloys and composites, the experiments carried out in this work provide a route to investigate the corrosion problems on a real atomic-scale, which can also be applied to relevant studies.

## 2. Material and methods

The  $\text{B}_4\text{C}/\text{Al}$  composite was fabricated by powder metallurgy technique using alloy powders with nominal composition of  $\text{Al}-1.0\text{Mg}-0.65\text{Si}-0.5\text{Cu}$  (wt.%) as the matrix and  $\text{B}_4\text{C}$  particles (21 wt.%) with an average diameter of  $\sim 7\ \mu\text{m}$  as the reinforcements. The as-mixed alloy and  $\text{B}_4\text{C}$  powders were cold pressed in a cylindrical die under a pressure of 50 MPa and then hot pressed at  $620\ ^\circ\text{C}$  under a pressure of 30 MPa for 2 h, producing the composite billets. The hot-pressing temperature ( $\sim 620\ ^\circ\text{C}$ ) was chosen to be a little higher than the melting point ( $600\ ^\circ\text{C}$ ) of the alloy matrix to produce a certain quantity of interfacial reaction products. The billets were hot forged at  $450\ ^\circ\text{C}$ . The forged samples were solution treated at  $530\ ^\circ\text{C}$  for 2.5 h, water quenched and then aged at  $175\ ^\circ\text{C}$  for 6 h.

Low magnification TEM characterizations, including bright field (BF) imaging, selective-area electron diffraction (SAED), high-angle annular dark-field (HAADF) imaging and energy dispersive spectroscopy (EDS) analysis, were performed using FEI Tecnai  $\text{G}^2$  F30 microscope. The atomic-scale TEM observations and high-magnification EDS analysis were conducted by an FEI Titan Themis cubed  $\text{G}^2$  TEM equipped with a SuperX-EDS detector. The convergent semi-angle was set as 21.4 mrad, and the inner collection angle was 70 mrad. TEM specimens were prepared by regular method, i.e. mechanical polishing and ion-milling using Gatan PIPS 695.

*Quasi in-situ* TEM observations were carried out following the procedures: after the first-round TEM observation, the TEM specimen was taken out and then immersed into 3.5 % NaCl solution which is commonly used as the electrolyte to study pitting corrosion. The experiments were conducted at room temperature for various periods. After that, the corroded specimen was cleaned by distilled water, dried, and then moved to TEM for the second-round investigation. Before each

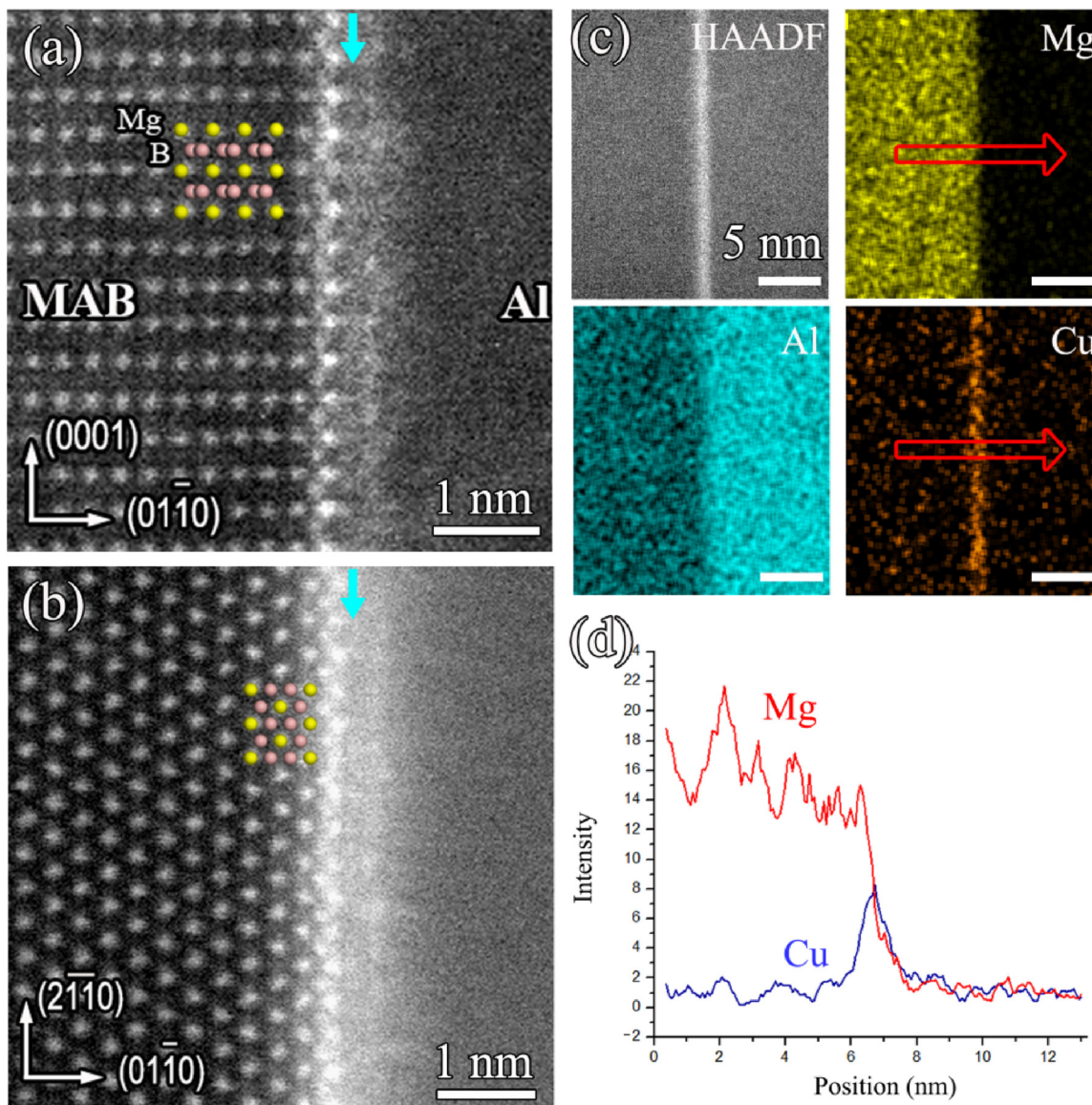


Fig. 2. (a) and (b) High resolution HAADF images of the Mg(Al)B<sub>2</sub> (labeled as MAB in the figure) nano-rod viewed along the [1̄210] and [0001] directions, respectively. The interfacial layer is marked by arrows. (c) and (d) EDS elemental maps of the interfacial layer and line profiles along the blank arrows in Mg and Cu maps, suggesting the enrichment of Mg and Cu in the interfacial layer.

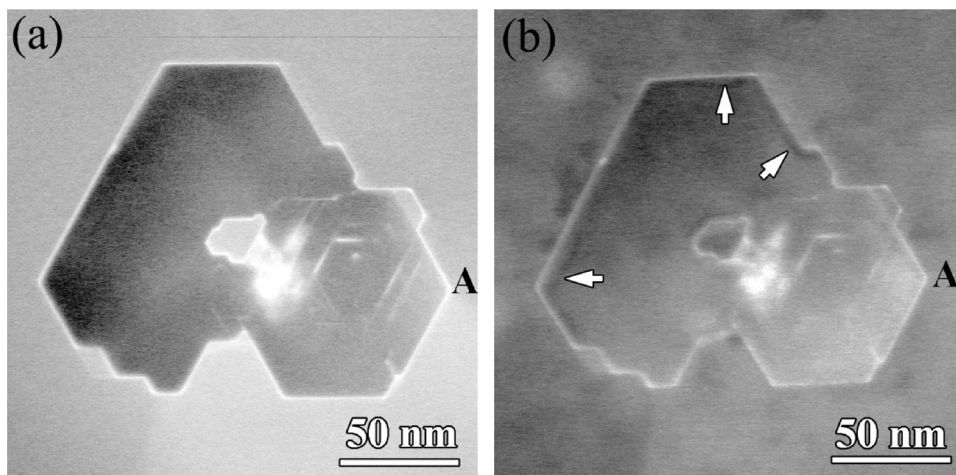
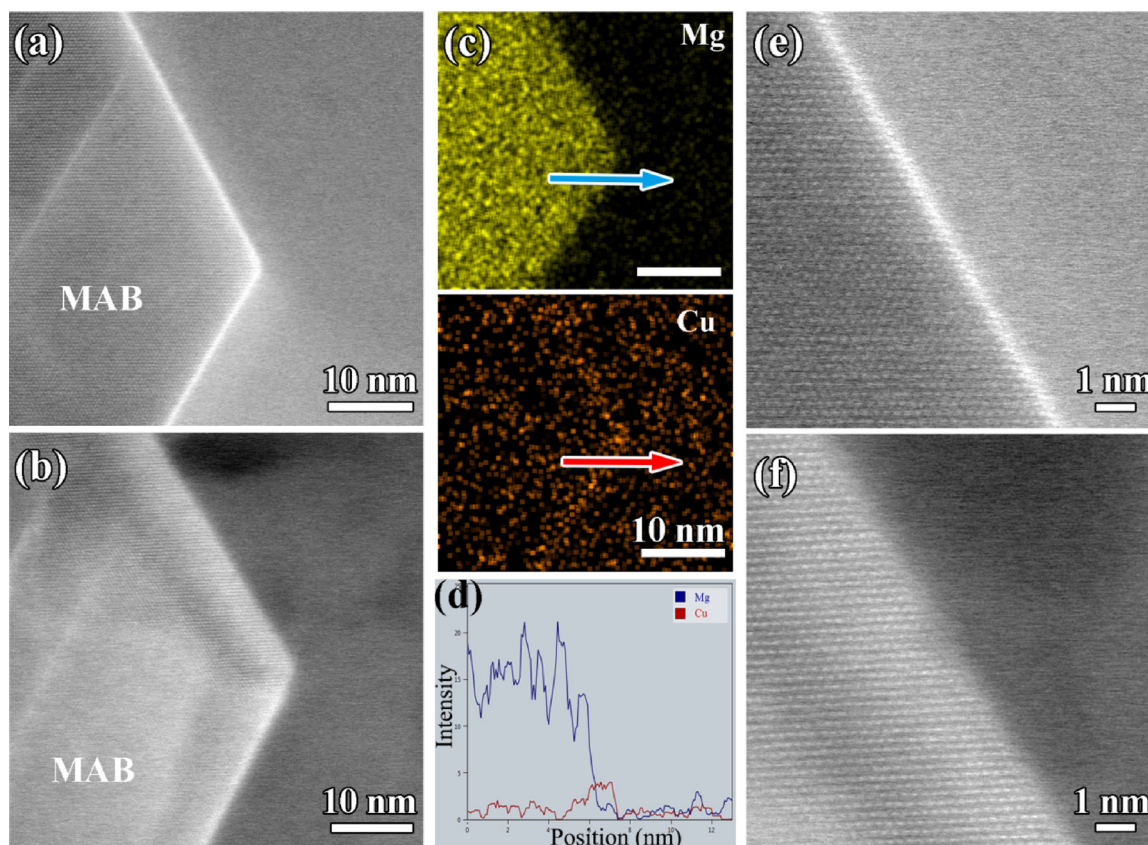


Fig. 3. (a) HAADF image of a coarse-size Mg(Al)B<sub>2</sub> nano-rod viewed along the [0001] zone-axis. (b) HAADF images of the Mg(Al)B<sub>2</sub> nano-rod but experienced 60 min immersion in 3.5 % NaCl. The pronounced bright contrast of the Cu-rich layer became weak after corrosion and dark strips appeared inside the Mg(Al)B<sub>2</sub> along its edges (arrowed).



**Fig. 4.** High magnification study of the degradation of the Mg(Al)B<sub>2</sub>/Al interface. (a) and (b) HAADF images of a corner part of the Mg(Al)B<sub>2</sub> shown in Fig. 3 before and after 60 min immersion in NaCl solution, respectively. Decomposition of the interfacial layer and the Mg(Al)B<sub>2</sub> along its edge can be clearly seen at the highly magnified view. (c) and (d) are the elemental maps and the corresponding line profiles along the red and blue arrows, showing the selective dissolution of Mg and a small amount of Cu remnant at the interface. (e) and (f) are the zoom-in images of the interface in (a) and (b). The interfacial layer became disordered because of dealloying in 3.5 % NaCl (For interpretation of the references to colour in this figure legend, the reader is referred to the web version of this article.).

round of observation, the specimen was plasma-cleaned to reduce the carbon contamination. In order to get a reliable comparison, the TEM investigations were performed when the interested secondary phases were tilted to a certain crystalline zone axis before and after the corrosion. At a higher magnification, finding back an exact location in the second round observation is challenging. Therefore, the locations with a special feature (for example, a corner) were particularly checked and compared to overcome the difficulty. To study the corrosion behaviors of the material suffered variant immersion periods, we conducted *quasi in-situ* experiments on newly prepared TEM specimens instead of studying the same area experienced progressive immersion times, since the local environment and corrosion product could be changed when the sample was taken out from solution, cleaned and dried. Moreover, 2 ~ 3 specimens suffered the same immersion period were characterized to make sure the observation was repeatable.

### 3. Results

The chemical reactions between B<sub>4</sub>C particles and the alloy matrix have been identified in our previous work [25]. A large number of Mg(Al)B<sub>2</sub> dispersoids, as one kind of the reaction products could be commonly seen in the alloy matrix. The BF TEM images in Figs. 1(a) and (b) show the two vertical projections of the nanocrystals along the [11 $\bar{2}$ 0] and [0001] zone-axis, respectively. The Mg(Al)B<sub>2</sub> nanocrystal usually possessed a rod shape in TEM images, with several tens of nanometers in diameter and several micrometers in length. They were called as Mg(Al)B<sub>2</sub> nano-rods for convenience herein. To better understand the corrosion morphologies associated with the Mg(Al)B<sub>2</sub> dispersoids in the following, the 3D configuration of the nanocrystals should be figured

out. Combining the two vertical shapes shown here and in other observations, it was known that these nano-rods were actually prisms and the prismatic surfaces were  $\langle 10\bar{1}0 \rangle$  planes. An ideal configuration should be a hexagonal prism with six exposed  $\langle 10\bar{1}0 \rangle$  facets. When the compound grew and coarsened ( $> 100$  nm in diameter), more  $\langle 10\bar{1}0 \rangle$  surfaces would be formed and result in a polyhedral prism shape. EDS quantitative analysis performed on several tens of the compounds suggested that they were composed of Mg, Al ( $Mg_{at}:Al_{at} \approx 1:1$ ) and B.

Instead of forming strengthening precipitates, alloying element Cu in the composite was found to segregate at the Mg(Al)B<sub>2</sub>/Al interfaces. The EDS elemental mapping performed on the Mg(Al)B<sub>2</sub> nano-rod in Fig. 1(b) is given in Fig. 1(c). The Cu enrichment is clear seen at the periphery of the nano-rod.

The high-resolution HAADF images further revealed the details of the Cu-rich layer at the interface. To get high quality micrographs, the Mg(Al)B<sub>2</sub> nanocrystals located at the very thin areas in a TEM foil were chosen to observe. Figs. 2(a) and (b) are the side view and top view of the Mg(Al)B<sub>2</sub>/Al-matrix interface, respectively. HAADF image mode provides the 'Z contrast' which is in proportion to the total atomic numbers along an atomic column. The bright layer adjacent to Mg(Al)B<sub>2</sub> (denoted by blue arrows) should contain heavy element, i.e. Cu in the present sample. The Cu-rich layer was nearly 1 nm in thickness. Since no definite crystalline orientation relationship (OR) existed between Mg(Al)B<sub>2</sub> and the aluminum matrix, the latter did not show any crystalline lattice. It is noted that the atoms in the Cu-rich layer seem to be regularly arranged and form a crystalline-like structure (one or two unit cells) in both the projections in Figs. 2(a) and (b). Unfortunately, the limited size made the precipitates very difficult to be identified. It could only be sure that the heavy atoms occupied both the positions of

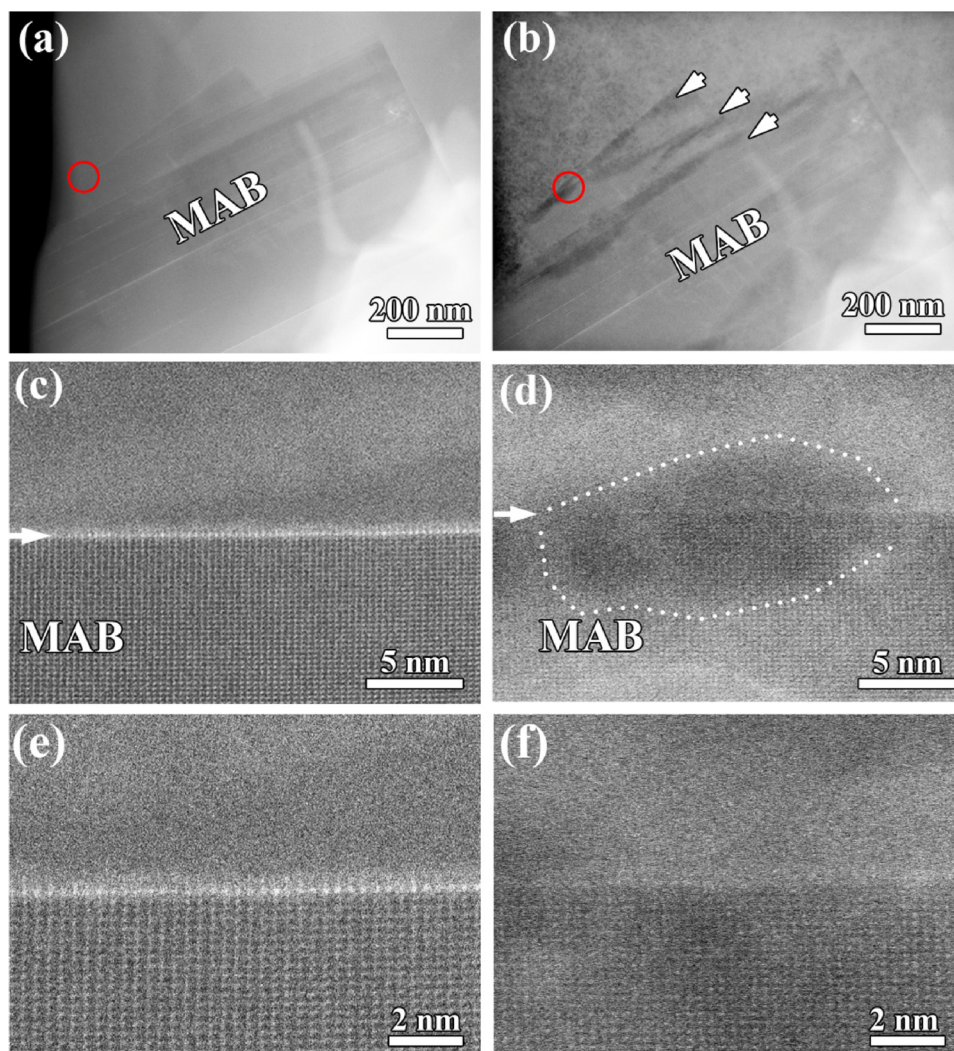


**Fig. 5.** *Quasi in-situ* TEM characterization of the Mg(Al)B<sub>2</sub>/Al interface degradation along the  $[1\bar{2}10]_{\text{Mg(Al)B}_2}$  direction. (a) and (b) are HAADF images of a Mg(Al)B<sub>2</sub> nano-rod before and after 60 min immersion in 3.5 % NaCl solution, respectively. The dark strips along the interfaces in (b) are denoted by white arrows. The interface marked by red circles are observed at a higher magnification and shown in (c) and (d). The dark area enclosed by the dot line is heavily attacked. Inside the pit, the Cu-rich interfacial layer was almost removed. (e) and (f) show a section of interface near that in (c) and (d). The regular lattice of the interfacial layer in (e) was destructed after the immersion and only a faint contrast remained (For interpretation of the references to colour in this figure legend, the reader is referred to the web version of this article).

Mg(Al) and B columns in the very inner atomic plane adjacent to the Mg(Al)B<sub>2</sub>. The interfacial layer was also analyzed by the high-resolution EDS mapping displayed in Fig. 2(c). In addition to Cu, this layer contained a certain amount of element Mg, as indicated by the line profile (Fig. 2(d)) across the interface in Fig. 2(c). The signal of Mg almost dropped at the same point as Cu did. The result suggested that this layer was a Cu/Mg-rich compound. The atomic ratio of Cu<sub>at</sub> : Mg<sub>at</sub> was roughly calculated to be 1:2. However, the exact values of the elements contained in this atomic-scale layer were not easy to acquire. A similar metallic 2-dimensional compound (2DC) was also found on the TiB<sub>2</sub> surfaces which served as grain refiner in Al-Ti alloys [31].

To trace the compositional and structural evolutions associated with the Mg(Al)B<sub>2</sub> dispersoids at the very beginning of corrosion process, *quasi in-situ* TEM observations were performed. Fig. 3(a) shows a HAADF image of a Mg(Al)B<sub>2</sub> nano-rod viewed along its [0001] direction. As mentioned before, the coarsened Mg(Al)B<sub>2</sub> crystal possessed a complex configuration and more than 20  $\langle 10\bar{1}0 \rangle$  prismatic facets were contained in the present case. The Cu/Mg-rich layer surrounding it showed brighter contrast compared with the neighbor Al matrix. After immersion in 3.5 % NaCl for 60 min, the same area in Fig. 3(a) was found and characterized (Fig. 3(b)) under the same conditions as before

(including the specimen tilting angles and imaging conditions). Direct comparison of the micrographs in Figs. 3(a) and (b), the differences in between could be observed as follows: (i) The contrast of the interfacial Cu-rich layer was weakened after the immersion test. (ii) A thin dark strip appeared inside the Mg(Al)B<sub>2</sub> along its edges (the Mg(Al)B<sub>2</sub>/Al interfaces) as marked by white arrows in Fig. 3 (b). The contrast changes in the HAADF image represented the dissolution or decomposition of the local areas.

More details were able to be revealed by *quasi in-situ* examination on the Mg(Al)B<sub>2</sub>/Al interfaces at a high magnification. The corner of the Mg(Al)B<sub>2</sub> prism denoted by 'A' in Figs. 3(a) and (b) is shown in Figs. 4(a) and (b). The thin strip along the interface with different contrast was clearly seen in the Mg(Al)B<sub>2</sub> after the immersion. In addition, when the atom columns in the strip were clearly imaged at an optimal defocus value, the other areas became blurred, which suggested the thickness change in the dark strip. In comparison, we could see that the whole area of the Mg(Al)B<sub>2</sub> in Fig. 4(a) is quite uniform at the same defocus condition. Therefore, it is clearly pointed out that the degradation of Mg(Al)B<sub>2</sub> took place from the edge. On the other hand, the contrast change of the interfacial layer was more evident at the highly magnified view. In Fig. 4(b), it is seen that the Cu-rich layer in the lower

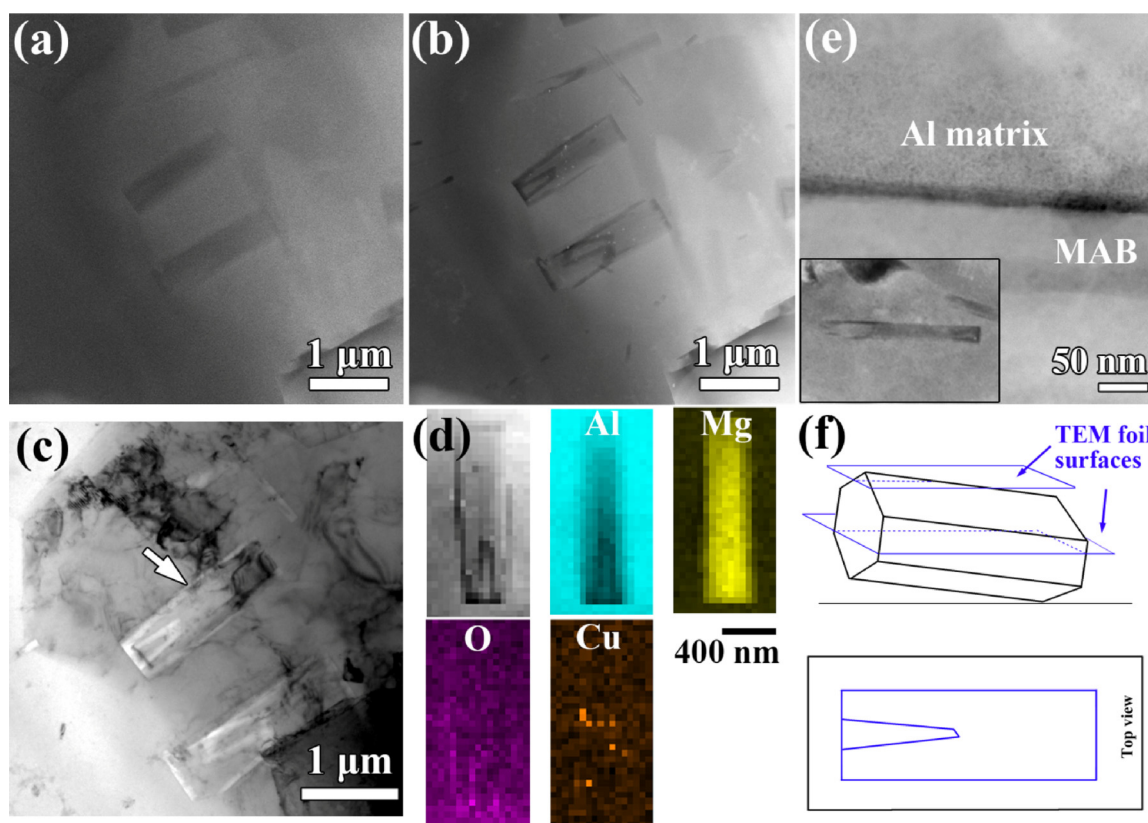


**Fig. 6.** (a) HAADF image showing several Mg(Al) $B_2$  nano-rods embedded in the aluminum matrix. (b) The same area in (a) but after immersion in NaCl solution for 90 min. The nano-rods are outlined by narrow corrosion trenches along their edges. (c) Bright-field (BF) TEM image of the degraded Mg(Al) $B_2$  nano-rods. The trenching areas become more electron-beam transparency due to the thickness reduction. (d) EDS elemental mapping of the Mg(Al) $B_2$  nano-rod denoted by an arrow in (c). (e) A high magnification image of the corrosion trench at the interphase boundary. The width of the trench is in the range of 20 ~ 30 nm. (f) Schematic illustration of a sloped Mg(Al) $B_2$  nano-rod (hexagonal prism) embedded in a TEM foil (above) and the projection of the Mg(Al) $B_2$ /Al interfaces exposed on the foil surfaces (below). The projection was exactly the same as the morphology of corrosion trenches at the periphery of the Mg(Al) $B_2$  in (d).

part of the corner becomes much weak while the layer in the upper part is almost vanished. Fig. 4(c) shows the Mg and Cu maps of the corner area. The Cu contained in the interfacial layer was indeed very dilute. In addition, according to the line profile (Fig. 4(d)) across the interphase boundary along the arrow direction in Fig. 4(c), the content of Mg at the point where Cu concentrated was decreased to the same level as that in the matrix. The observations tended to suggest that the destruction of the interfacial layer was due to the selective dissolution of element Mg. The Cu remnant was also to some extent released from the layer.

The atomic-scale morphology of the Mg(Al) $B_2$ /Al interface was examined through the zoom-in images in Figs. 4(e) and (f). They were taken from the same area near the corner shown in Figs. 4(a) and (b). The destruction of the interfacial layer could be seen by the disordered interphase boundary in Fig. 4(f) in comparison with that in Fig. 4(e).

The hidden information due to the 2D projection nature of TEM images potentially leads to some misunderstanding of the degradation process. We therefore carried out *quasi in-situ* observations along the vertical direction of the Mg(Al) $B_2$  nano-rod. Fig. 5(a) shows a coarse-size Mg(Al) $B_2$  nano-rod viewed along the  $[1\bar{2}10]$  zone axis. The multiple prismatic facets could be identified according to the contrast variation paralleled to the  $c$ -axis. The same area suffered 60 min immersion in NaCl solution was examined (Fig. 5(b)). As denoted by arrows, several dark strips paralleled to the  $[0001]$  direction appeared inside the Mg(Al) $B_2$ . High resolution HAADF images of the pristine interface and the same area after corrosion are displayed in Figs. 5(c) and (d). The degradation characteristics resembled that in Fig. 4. Specifically, the loss of the interfacial Cu-rich layer and the decomposition of Mg(Al) $B_2$  along the interface were observed. Judging from the contrast and

imaging defocus, the dark area enclosed by dot line in Fig. 5(d) should be the heavily corroded area. Inside the pit, the Cu-rich layer almost all dissolved, whilst some residual bright contrast could also be seen along the interface outside the pit. The interface area near the pit was also compared at a higher magnification as shown in Figs. 5(e) and (f). The pristine interfacial layer showed visible crystalline lattice as we presented in Fig. 2. After 60 min immersion, no regular lattice but only some faint contrast could be seen at the interface. The result agreed well with that in Fig. 4 and further suggested the Mg(Al) $B_2$  decomposition promoted the dealloying of the interfacial layer going deeper.

Figs. 6(a) and (b) display the micrographs of several Mg(Al) $B_2$  nano-rods in the aluminum matrix before and after 90 min immersion in NaCl solution. Extended immersion in NaCl solution yielded evident trench formed along the Mg(Al) $B_2$ /Al interface, as shown as the black strip induced by thickness change around the Mg(Al) $B_2$  nano-rods in the HAADF image in Fig. 6(b). The area was also characterized by BF TEM and EDS analysis. Due to the thinning of the local areas, the corrosion trench was more electron-beam transparency in the BF condition (Fig. 6(c)). The elemental maps of the Mg(Al) $B_2$  nano-rod marked by an arrow in Fig. 6(c) are shown in Fig. 6(d). The signal intensities of Mg and Al became lower in the corroded areas and the O signal appeared, conforming the decomposition of Mg(Al) $B_2$ . Moreover, the Cu signal could no longer be detected at the interfacial area. Instead, it appeared at some locations on the Mg(Al) $B_2$  nano-rod. The Cu redistribution will be discussed later. A high magnification image of the corrosion trench at the phase boundary is shown in Fig. 6(e). The area was taken from the inset image. The steep dark contrast indicated a narrow (20 ~ 30 nm in width) and deep trench formed at the interface. The whole Cu-rich layer was completely removed.

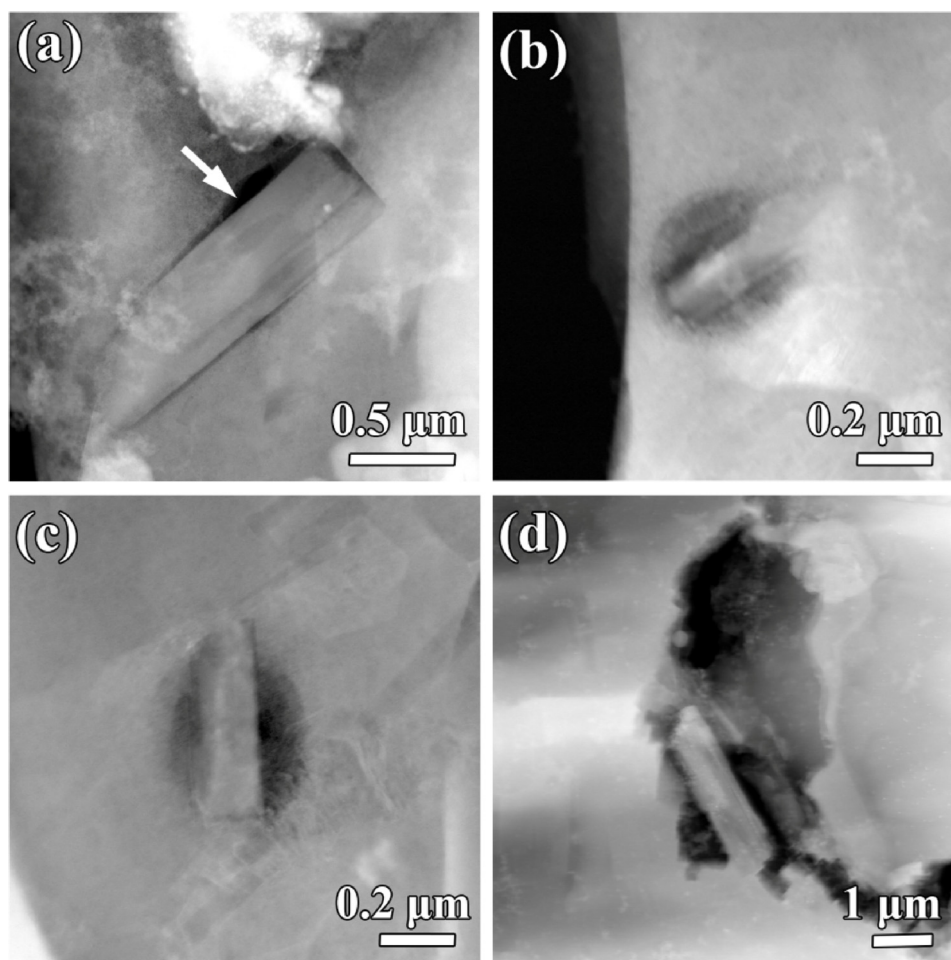


Fig. 7. HAADF images of the pitting corrosion associated with the  $\text{Mg}(\text{Al})\text{B}_2$  nano-rods in the sample suffered 90 min ~ 100 min immersion in 3.5 % NaCl.

One may notice that the corrosion strips also developed 'inside' the  $\text{Mg}(\text{Al})\text{B}_2$  nano-rods. In fact, these strips were along the  $\text{Mg}(\text{Al})\text{B}_2/\text{Al}$  interfaces projected onto the image plane. It would be understandable by the help of the schematic illustration in Fig. 6(f). According to the EDS maps in Fig. 6(d), the Al signal in the upper part of the  $\text{Mg}(\text{Al})\text{B}_2$  nano-rod was higher than that in the lower part. This variation was resulted from the overlapped Al matrix. In other words, the nano-rod gently sloped at a small angle from the TEM foil surface. Considering that a sloped hexagonal prism (embedded in the Al matrix) was polished on both upper and lower sides, leaving the part in between the two horizontal planes *i.e.* the top and bottom surfaces of a TEM foil, we could get the projection of the  $\text{Mg}(\text{Al})\text{B}_2/\text{Al}$  interfaces onto the foil plane as the pattern shown in Fig. 6(g) (image below). The contour was exactly the same as the morphology of corrosion trenches associated with the  $\text{Mg}(\text{Al})\text{B}_2$  nano-rod in Fig. 6(d). It means that the degradation only occurred along the  $\text{Mg}(\text{Al})\text{B}_2/\text{Al}$  interfaces initially, while the larger area of the  $\text{Mg}(\text{Al})\text{B}_2$  surface exposed to electrolyte has not been attacked.

Conceivably, the formation of corrosion trenches would expose the fresh metal matrix to the aggressive environment. As a consequence, the corrosion propagated towards the aluminum matrix. It was confirmed by more experimental findings in the samples experienced 90 min ~ 100 min immersion in NaCl solution. Fig. 7 gives several examples showing the expanded corrosion pits in the vicinity of  $\text{Mg}(\text{Al})\text{B}_2$  dispersoids. From Fig. 7(a) through Fig. 7(d), the pits with different scales are exhibited. Nevertheless, the  $\text{Mg}(\text{Al})\text{B}_2$  dispersoids inside the pits were not severely dissolved and almost maintained their original shapes.

With prolonged immersion period to 120 min, the corrosion was severely spread in the aluminum matrix. Inside the attacked areas, the  $\text{Mg}(\text{Al})\text{B}_2$  could be frequently found as well. Fig. 8 shows the  $\text{Mg}(\text{Al})\text{B}_2$  nanocrystals left inside the corrosion pit. EDS mapping indicated that these nanocrystals were enclosed by the outside oxide layer, while the inner part was composed of Mg, Al and B. Taking a close inspection on the edge of a  $\text{Mg}(\text{Al})\text{B}_2$  nano-rod, we could find that an amorphous shell with a thickness of 5 nm covering it and the interior remained the crystalline feature since the atomic columns were recognized. EDS analysis indicated that the shell was composed of Mg, Al and O. The finding indicated that the  $\text{Mg}(\text{Al})\text{B}_2$  nano-rod underwent dissolution at the beginning but became chemically stable by forming the magnesium (aluminum) oxide shell.

In addition to the  $\text{Mg}(\text{Al})\text{B}_2$  compound,  $\text{Al}_3\text{BC}$  particle was also produced via the reaction between  $\text{B}_4\text{C}$  and aluminum. Fig. 9(a) is a BF TEM image showing the  $\text{Al}_3\text{BC}$  particle located at the periphery of a  $\text{B}_4\text{C}$  particle. This compound has an *hcp* structure with  $a = 0.35$  nm,  $c = 1.15$  nm (see the electron diffraction pattern inset). HAADF image in Fig. 9(b) and EDS mapping in Fig. 9(c) prove a Cu-rich layer at the boundary between  $\text{Al}_3\text{BC}$  particle and the aluminum matrix. The Mg map indicated that the element was also contained in the compound ( $\text{Mg}_{\text{at}}/\text{Al}_{\text{at}} \sim 10\%$ ) and in the interfacial layer. The highly magnified HAADF imaging in Fig. 9(d) indicates the thickness of the layer being about 1 nm. A regular arrangement of the segregated atoms was indistinctly visible. It was not clear whether the layer had a well crystallized structure as the one at the  $\text{Mg}(\text{Al})\text{B}_2/\text{Al}$  interface based on the image of the layer in Fig. 9(d).

*Quasi in-situ* observation was carried out on an  $\text{Al}_3\text{BC}$  particle, as

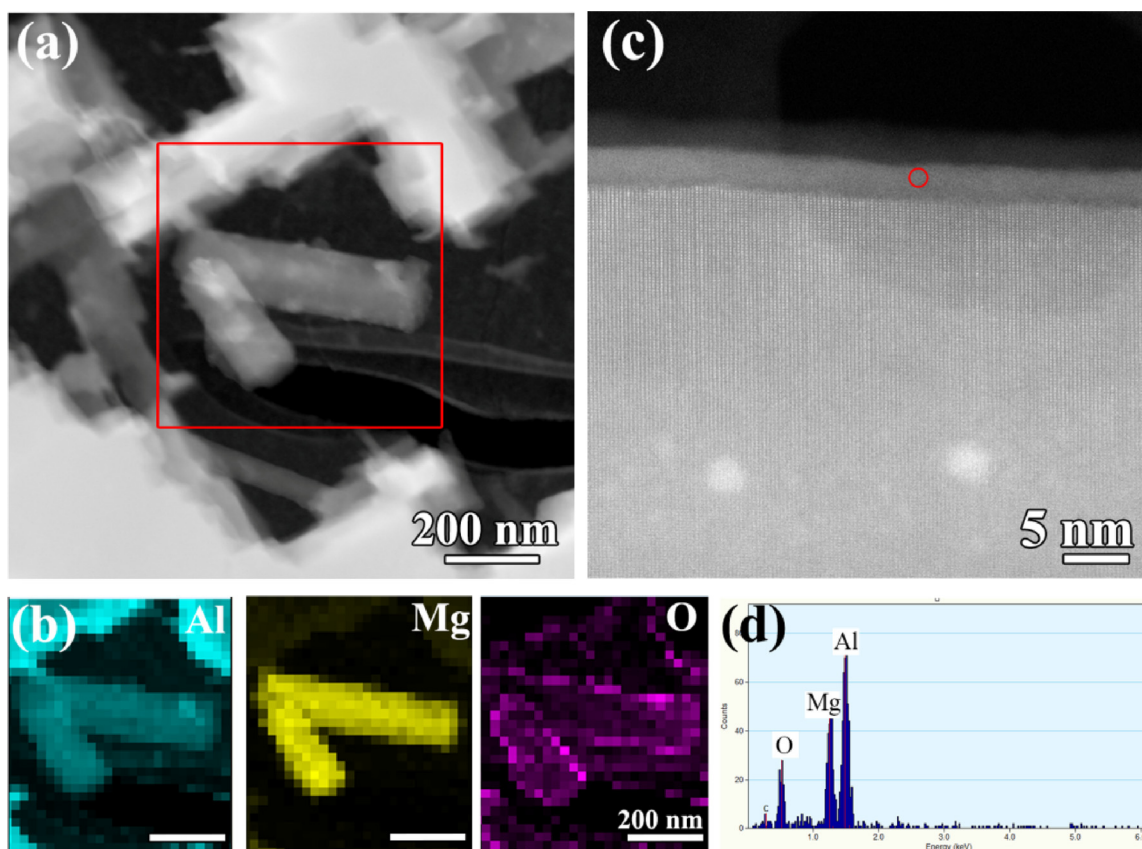


**Fig. 8.** (a) HAADF image of the severely attacked aluminum matrix after 120 min immersion in NaCl. Inside the corrosion area, two Mg(Al)B<sub>2</sub> nano-rods are seen. (b) EDS elemental mapping showing an oxygen-rich shell over the surface of the Mg(Al)B<sub>2</sub> nano-rod. (c) High resolution HAADF image of the edge of a Mg(Al)B<sub>2</sub> nano-rod. The crystalline Mg(Al)B<sub>2</sub> nano-rod is covered by an amorphous thin film with about 5 nm in thickness. (d) EDS analysis on the amorphous layer suggesting it is composed of Mg, Al and O.

shown in Fig. 10. Figs. 10(a) and (b) are the same area before and after 90 min immersion in NaCl solution, respectively. The Al<sub>3</sub>BC/Al interface arrowed in Fig. 10(a) was investigated by high resolution HAADF STEM, as displayed in Fig. 10(c). After the immersion, the destructed interfacial layer (Fig. 10(d)) exhibited weaker contrast. The EDS mapping revealed that the Cu signal in the layer was still present although not as strong as that in Fig. 9(b), but the Mg was almost absent. It is worth noting that even when we prolonged the immersion time to 120 min which was enough for the heavy corrosion of the alloy matrix near Mg(Al)B<sub>2</sub> dispersoids, we did not observe complete dissolution of Cu at the Al<sub>3</sub>BC/Al boundaries and the following trench formation, as that taking place at the Mg(Al)B<sub>2</sub>/Al boundaries.

The above results unambiguously demonstrated that the interfacial layer adjacent to the Mg(Al)B<sub>2</sub> or Al<sub>3</sub>BC compound in the composite was preferentially dissolved at the very initial stage of corrosion. Meanwhile, it was also noticed the redistribution of Cu on the Mg(Al)B<sub>2</sub> nano-rod in Fig. 6(d). In the following, the redistributed Cu particles were characterized.

Fig. 11(a) is a HAADF image showing the Mg(Al)B<sub>2</sub> nano-rods were decorated by a mass of nano-sized (20 ~ 50 nm) bright particles. The chemical composition of the area framed in Fig. 11(a) was characterized by EDS elemental mapping (Fig. 11(b)). The high O signals were mainly detected from the corrosion trench, while the Cu was only from the nano-particles, suggesting they were metallic Cu particles. The pronounced Cu signal from the nano-particles could also be seen from the EDS spectrums collected from the point 1 and point 2 labeled in the Cu map.

It was also observed that the B<sub>4</sub>C reinforcements were covered by Cu nano-particles. Fig. 12(a) shows a B<sub>4</sub>C particle in the specimen suffered 90 min immersion in NaCl solution. The Cu nanoparticles

dispersed upon B<sub>4</sub>C could be clearly seen in the zoom-in image inset. The elemental maps of the area suggested these particles contained Cu but no oxygen (Fig. 12(b)). High resolution TEM image on a single nanoparticle and the Fast Fourier transformation (FFT) pattern derived from the micrograph are shown in Fig. 12(c). The FFT pattern can be indexed by the diffraction of metallic Cu. The nanoparticle was made up of randomly oriented fine clusters, as seen in the HRTEM image and the diffraction rings in the FFT pattern. The characteristics indicated that the nano-particles formed via redeposition of Cu ions.

#### 4. Discussion

Interfacial segregation of solute atoms is prevalent in ceramic particles-reinforced AMCs. Strangwood et al. [17] reported the solute segregations, such as Mg, Cu, and Zn, at SiC/Al interfaces in 2xxx and 7xxx Al based AMCs. Ma et al. [32] found the interfacial enrichment of Cu in the AMC reinforced by in-situ AlN. In a similar case, the grain refiner, i.e. in-situ formed TiB<sub>2</sub> particle which is often used in aluminum alloys, was also found to be enclosed by a Zr-rich atomic layer in an Al-Zr alloy [33]. To date, seldom attention has been paid to their electrochemical and/or chemical effects on the corrosion behavior of materials.

The present work focused on the distribution of alloying element Cu in a B<sub>4</sub>C/Al composite and its corrosion response when the composite was immersed in NaCl solution. The element Cu in addition to Mg were found at the periphery of Mg(Al)B<sub>2</sub> and Al<sub>3</sub>BC compounds which were in-situ formed by the chemical reactions between B<sub>4</sub>C and the alloy matrix during fabrication. High resolution TEM characterization indicated that the enriched elements formed a crystalline-like compound at the Mg(Al)B<sub>2</sub>/Al interface. The *quasi in-situ* TEM observations

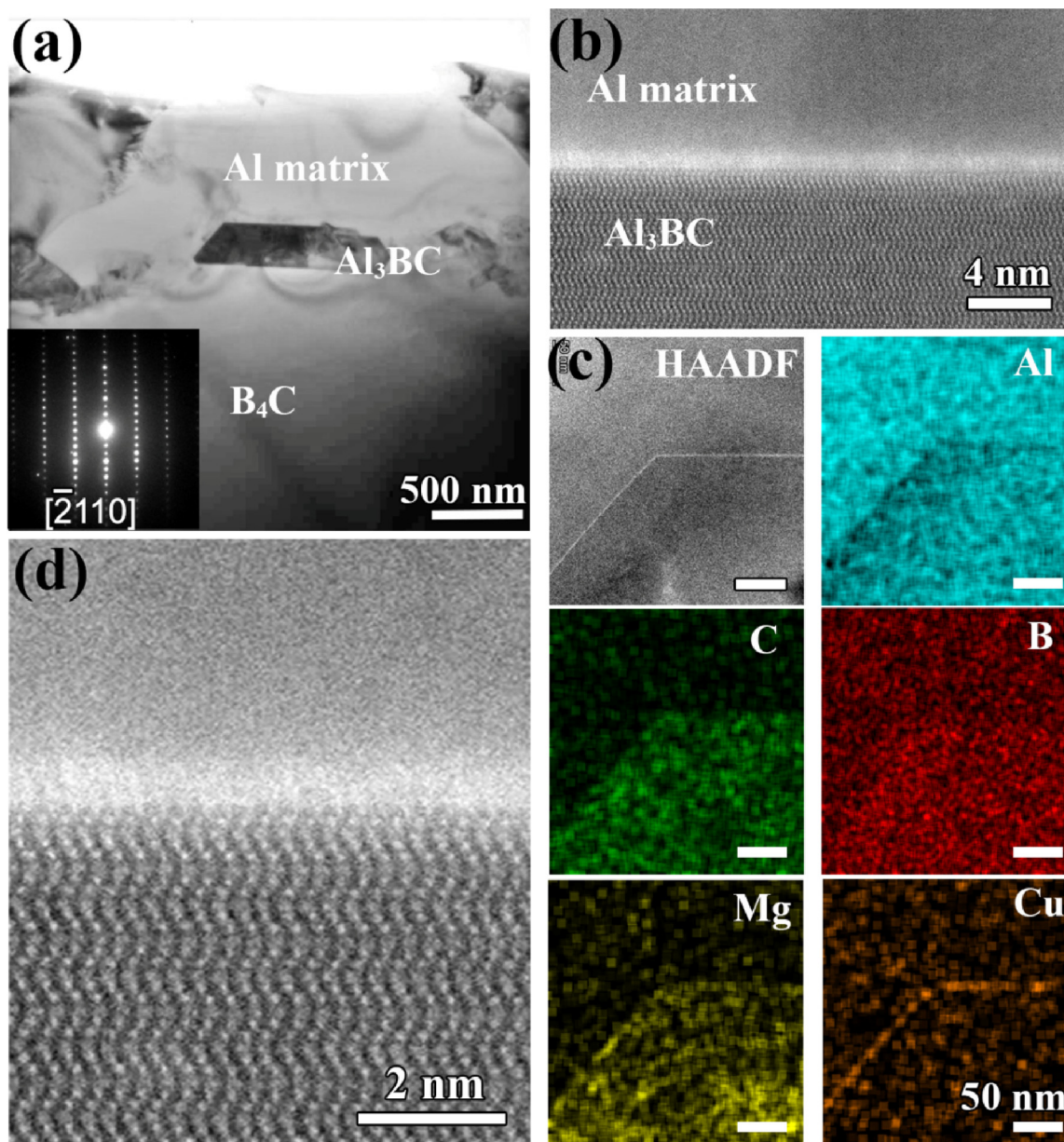


**Fig. 9.** Characterization of the Cu enrichment at the Al<sub>3</sub>BC/Al interface. (a) Bright-field TEM image of an Al<sub>3</sub>BC nano-particle located at the periphery of a B<sub>4</sub>C particle. Inset is the corresponding SAED pattern of the Al<sub>3</sub>BC. (b) High resolution HAADF image of the Al<sub>3</sub>BC/matrix interface showing the bright contrast at the interphase boundary. (c) Elemental maps showing the enrichment of Cu and Mg in the interfacial layer. (d) A high magnification image of the interfacial layer which shows some lattice pattern.

indicated that the Cu/Mg-rich layers at the interphase boundaries underwent dealloying before the occurrence of stable pitting in the composite.

We proposed that the present case was very similar to the behavior of S-Al<sub>2</sub>CuMg phase in NaCl [34,35], although the galvanic relationship between the Cu/Mg-rich layer and the aluminum matrix in the present composite was not clear owing to that the exact composition and structure of the layer were unknown. Nevertheless, Mg is an electrochemically active element and easily dissolves preferentially even in the cathodic Q-phase in a 6xxx Al alloys. Following the Mg dissolution, it was demonstrated that Cu clusters may become detached from the Cu-rich remnant. Due to the positive OCP of Cu in a chloride solution in comparison to its equilibrium potential ( $E_{Cu}$ ), oxidation of Cu and generation of Cu ions are possible. Analogous non-Faradaic liberation of Cu was also reported in Q-AlMgSiCu phase and magnesium alloys [30,36].

As for the different corrosion propagation associated with Mg(Al)B<sub>2</sub> and Al<sub>3</sub>BC compounds in the present case, we discussed the situations separately in the following.

The equilibrium potential of Mg(Al)B<sub>2</sub> in NaCl is still unknown, therefore it is not easy to theoretically predict its galvanic effect on the aluminum matrix. Pohlman [37] measured the galvanic currents between extracted boron fibers from both 2024 and 6061 AMCs and aluminum alloy. He demonstrated the interfacial reaction products, aluminum boride, but not the fiber itself, could give rise to the galvanic coupling with Al alloys. Although the composition of the boride was not characterized in his work, it was expected that Mg/Al containing borides were produced in 6061 AMC, since the binding energies for Al/B and Mg/B are similar [38]. Based on the data, the Mg(Al)B<sub>2</sub> compound should serve as cathodic sites in the Mg(Al)B<sub>2</sub>/Al system. Furthermore, the observations in Fig. 7 indeed supported the galvanic corrosion of the aluminum matrix associated with Mg(Al)B<sub>2</sub> dispersoids.

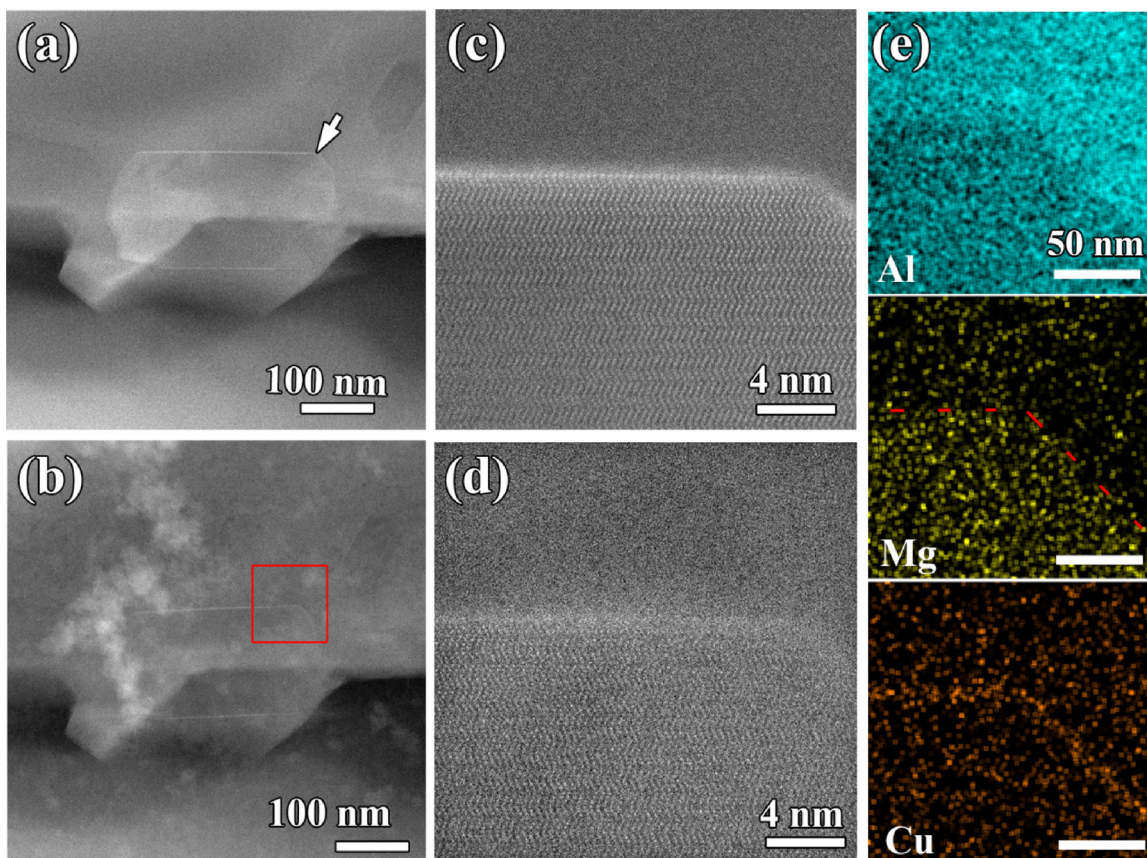


**Fig. 10.** Dealloying of the interfacial layer adjacent to  $\text{Al}_3\text{BC}$  particle in 3.5 % NaCl. (a) and (b) Low magnification HAADF images of the  $\text{Al}_3\text{BC}$  nano-particle before and after 90 min immersion, respectively. (c) and (d) are high resolution images of the arrowed interface in (a) before and after the immersion. The destruction of the interfacial layer is similar to that observed at the  $\text{Mg}(\text{Al})\text{B}_2/\text{Al}$  interface. (e) The elemental maps of the framed area in (b). The depletion of Mg and the Cu remnant in the interfacial layer can be seen from the maps. The location of the interphase boundary in the Mg map is marked by the dash line.

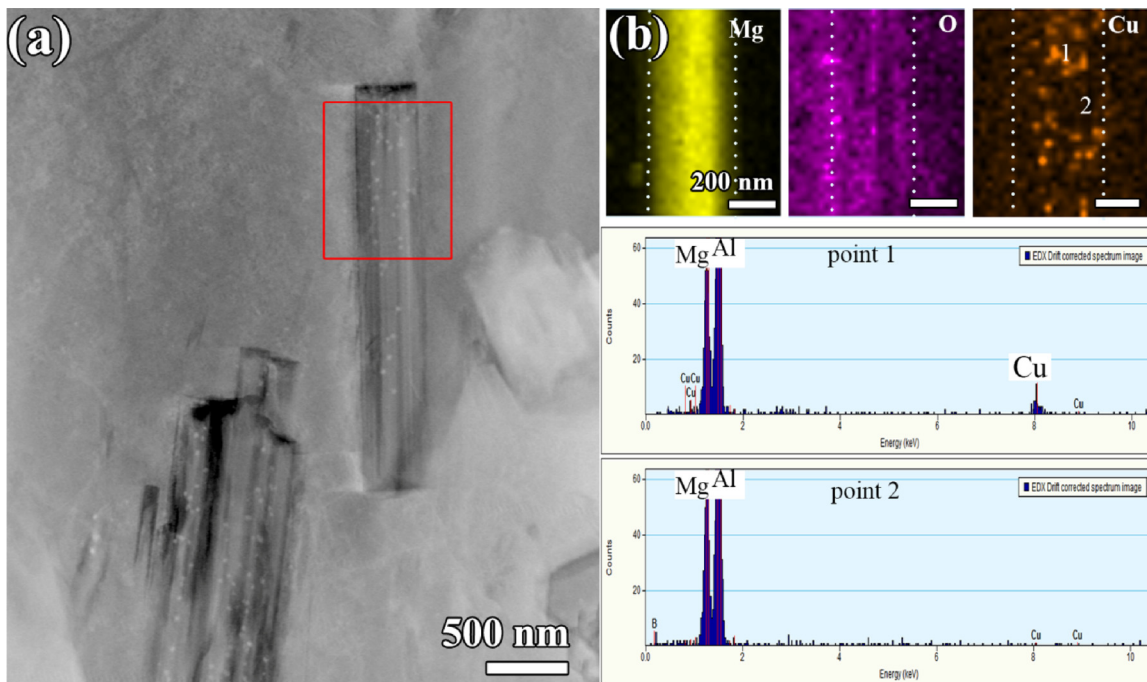


**Fig. 11.** (a) HAADF image showing the  $\text{Mg}(\text{Al})\text{B}_2$  nano-rods around which the corrosion trenches has formed (90 min immersion in 3.5 % NaCl). The  $\text{Mg}(\text{Al})\text{B}_2$  nano-rods are decorated by a mass of nano-sized Cu particles. (b) Element maps of the framed area in (a). O is enriched in the interfacial trenches. Only Cu signal is detected from the nano-particles upon the  $\text{Mg}(\text{Al})\text{B}_2$ . The corresponding EDS spectrums taken from the point 1 and point 2 in Cu map are also given.

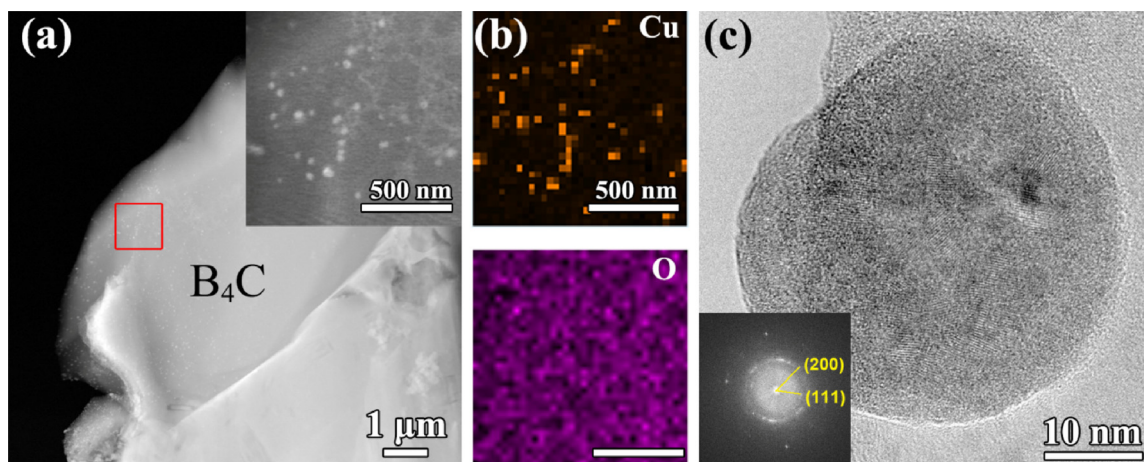


Fig. 12. (a) HAADF image showing the deposited Cu nano-particles upon a  $B_4C$  particle (90 min immersion in 3.5 % NaCl). The zoom-in image of the framed area is shown inset. (b) Cu and O maps of the same area in the inset in (a). (c) HRTEM image and the corresponding FFT pattern of a single Cu particle, indicating the particle consists of a number of fine clusters with random orientations.

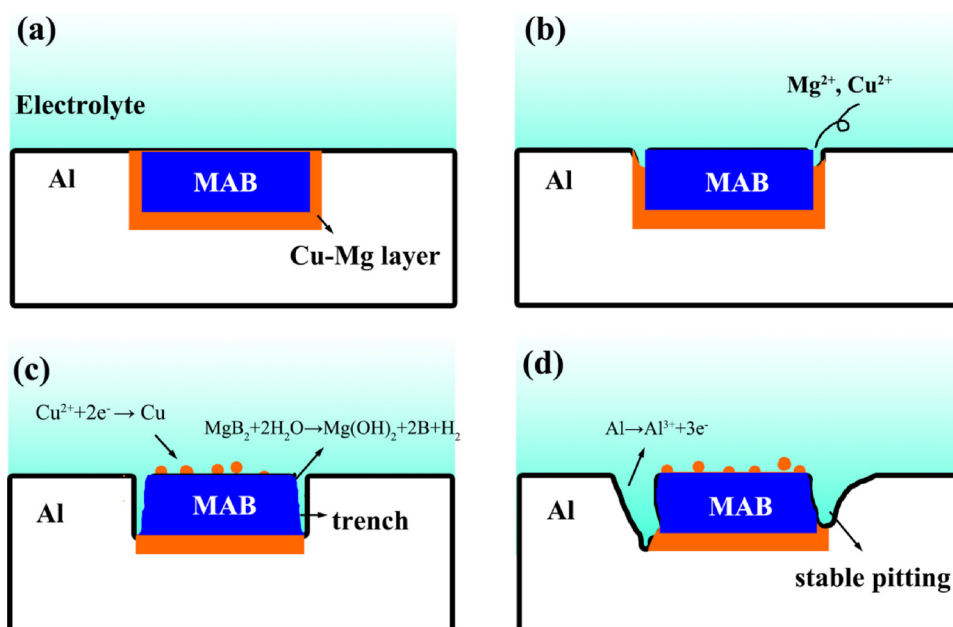


Fig. 13. A schematic illustration of the corrosion process associated with the  $Mg(Al)B_2$  dispersoids. (a) The pristine composite immersed in NaCl solution. (b) Dealloying of the interfacial layer occurred, releasing Mg and Cu ions into solution. (c) Decomposition of the  $Mg(Al)B_2$  and corrosion trench formed along the interphase boundary. The Cu/Mg-rich layer completely dissolved. Meanwhile, Cu nano-particles were deposited upon the cathodic phase. (d) Corrosion propagated to the Al-matrix and stable pitting appeared.

A contradictory phenomenon in our experiments was that the decomposition of  $Mg(Al)B_2$  compound in prior to the pitting of aluminum. It can be rationalized that the  $Mg(Al)B_2$  underwent chemical decomposition in the aqueous solution. The process is illustrated in the schematic diagram in Fig. 13. At first, the  $Mg(Al)B_2$  surface exposed to air was covered by a thin oxide layer [39] and inhibited the contact with the solution. When the interfacial Cu/Mg compound was selectively dissolved as mentioned above, the fresh  $Mg(Al)B_2$  and metallic Al-matrix were exposed (Fig. 13(b)). Then the exposed  $Mg(Al)B_2$  reacted with water and generated magnesium (aluminum) hydroxide and free boron [40] (Fig. 13(c)). The present of oxygen signals in the decomposed area of the  $Mg(Al)B_2$  (Fig. 6) and the oxygen-rich shell over the nano-rod (Fig. 8) confirmed the reaction. The decomposition further promoted the dealloying of Cu/Mg compound going deeper and also the liberation of Cu remnant. As the process continued, a remarkable trench would form around the  $Mg(Al)B_2$  nano-rod (Fig. 13(c)). Nevertheless, the decomposition of the  $Mg(Al)B_2$  would not progress towards the inner part by the protection of surface hydroxide shell (Fig. 8). At the same time, the trench formation led to the fresh Al-matrix uncovered. Accelerated by the cathodic  $Mg(Al)B_2$  nano-rods, the metal

matrix was attacked and stable pitting initiated (Fig. 13(d)).

For the case of  $Al_3BC$ , it was comparatively stable in the solution. In the present and our previous work [15], we did not find the pitting event directly associated with the  $Al_3BC$  compound. However, dealloying of the Cu/Mg-rich layer adjacent to the  $Al_3BC$  particle was expected to occur as well. It could be supported by the structure change and the weakened EDS signals as displayed in Fig. 10. We proposed the process followed the aforementioned mechanisms, as shown in Fig. 13(b). However, dealloying of the interfacial layer developed in a slower rate than that of the layer adjacent to  $Mg(Al)B_2$  whose cathodic effect played a important role. Although the Cu remnant in the dealloyed layer could in turn serve as cathode, its effect is negligible in comparison with the  $Mg(Al)B_2$ . Therefore, almost no serious attack of the aluminum matrix could be found in our experiments.

Following the liberation of the Cu clusters or Cu ions, redeposition occurred upon the cathodic phases, consuming the electrons provided by the dissolution of Mg (Fig. 13(c)). The behavior was akin to those reports for other Cu-containing precipitates and alloy matrices [30,34–36]. The noble potential of Cu compared to Al rendered the nano-particles serve as potent sites for cathodic reactions. Moreover,

B<sub>4</sub>C is actually a low-efficiency catalyst for cathodic reaction when they are coupled with Al [12]. The noble Cu depositions upon B<sub>4</sub>C particles could enhance the local cathodic dynamics.

In the past decade, *quasi in-situ* TEM method has been developed and applied in corrosion research. The experiments were conducted in open circuit [27,28,41,42] or polarization conditions [43], then the specimens were characterized by TEM imaging and EDS/EELS (electron energy loss spectroscopy) mapping [29,44,45] by which the structural and chemical information before and after corrosion could be obtained. The *quasi in-situ* observations in this work revealed the structural evolution of the material at a real atomic resolution. The technology allows us to unravel the complexity of the corrosion process related to the Mg(Al)B<sub>2</sub> and Al<sub>3</sub>BC dispersoids in a B<sub>4</sub>C-reinforced Al-Mg-Si-Cu composite. Solute atoms segregation at interfaces, such as stacking faults, grain boundaries, interphase boundaries, etc., is significant in alloys and receives considerable attentions during the years [46–49]. Due to the resolution limitation of the conventionally used characterization approaches in corrosion research, the effects of the segregated atoms are still unknown yet. We believe the TEM experiments in the work provide a feasible approach to study the issue.

## 5. Conclusions

In the present work, we investigated the initial stage of pitting corrosion on a B<sub>4</sub>C/Al-Mg-Si-Cu composite. The distribution and behavior of the alloying element Cu were revealed by *quasi in-situ* TEM at an atomic level. Main conclusions are listed as follows:

1. Alloying element Cu preferred to segregate adjacent to the in-situ produced reinforcements Mg(Al)B<sub>2</sub> and Al<sub>3</sub>BC in the B<sub>4</sub>C/Al-Mg-Si-Cu composite. Cu and Mg combined and formed a crystalline-like compound as the interfacial layers.

2. Exposed to NaCl solution, selective dissolution of the Cu/Mg-rich layer at the interphase boundaries was revealed by *quasi in-situ* TEM experiments. Decomposition of the Mg(Al)B<sub>2</sub> along the edges promoted the dealloying process of the interfacial layer and further resulted in the narrow trench formed around Mg(Al)B<sub>2</sub> nano-rods. The following pitting corrosion in the aluminum matrix was found to initiate at the periphery of Mg(Al)B<sub>2</sub> nano-rods. On the contrary, dealloying of the Cu/Mg-rich layer at the Al<sub>3</sub>BC/Al interface did not hurt the corrosion resistance of the composite.

3. Liberated Cu clusters and/or ions were then redeposited upon Mg(Al)B<sub>2</sub> nano-rods and B<sub>4</sub>C particles. HRTEM observation revealed that the single Cu nano-particle consisted of randomly oriented clusters. The Cu deposit could enhance the local cathodic reactions and increase the corrosion rate of the composite.

## Data availability

The raw/processed data required to reproduce these findings cannot be shared at this time, as the data form part of another ongoing study.

## CRediT authorship contribution statement

**Y.T. Zhou:** Conceptualization, Investigation, Writing - original draft, Funding acquisition. **Y.N. Zan:** Investigation, Visualization. **Q.Z. Wang:** Investigation, Funding acquisition. **B.L. Xiao:** Conceptualization, Writing - review & editing. **Z.Y. Ma:** Conceptualization, Writing - review & editing, Funding acquisition. **X.L. Ma:** Writing - review & editing.

## Declaration of Competing Interest

The authors declare that they have no known competing financial interests or personal relationships that could have appeared to influence the work reported in this paper.

## Acknowledgements

This work is supported by the National Natural Science Foundation of China (NSFC) [grant number U1508216] and NSF of Liaoning Province [grant number 20180551101], and the research fund of SYNL [grant number L2019F15]. Mr. B. Wu and L.X. Yang of this laboratory are acknowledged for their technical support on TEM experiments.

## Appendix A. Supplementary data

Supplementary material related to this article can be found, in the online version, at doi:<https://doi.org/10.1016/j.corsci.2020.108808>.

## References

- [1] H.S. Chen, W.X. Wang, Y.L. Li, P. Zhang, H.H. Nie, Q.C. Wu, The design, microstructure and tensile properties of B<sub>4</sub>C particulate reinforced 6061Al neutron absorber composites, *J. Alloys Compd.* 632 (2015) 23–29.
- [2] A.V. Pozdniakov, V.S. Zolotarevskiy, R.Yu. Barkov, A. Lotfy, A.I. Bazlov, Microstructure and material characterization of 6063/B<sub>4</sub>C and 1545K/B<sub>4</sub>C composites produced by two stir casting techniques for nuclear applications, *J. Alloys Compd.* 664 (2016) 317–320.
- [3] P. Zhang, Y. Li, W. Wang, Z. Gao, B. Wang, The design, fabrication and properties of B<sub>4</sub>C/Al neutron absorbers, *J. Nucl. Mater.* 437 (2013) 350–358.
- [4] X.-G. Chen, Application of Al-B<sub>4</sub>C metal matrix composites in the nuclear industry for neutron absorber materials, in: N. Gupta, W.H. Hunt (Eds.), *Solidification Processing of Metal Matrix Composites*, TMS, USA, 2006, pp. 343–350.
- [5] Y. Han, D. Gallant, X.G. Chen, Investigation on corrosion behavior of the Al-B<sub>4</sub>C metal matrix composite in a mildly oxidizing aqueous environment, *Corrosion* 67 (2011) 115005-1–115005-11.
- [6] Y.M. Han, X.G. Chen, Corrosion characteristics of Al-B<sub>4</sub>C metal matrix composites in boric acid solution, *Mater. Sci. Forum* 877 (2016) 530–536.
- [7] V.A. Katkar, G. Gunasekaran, A.G. Rao, P.M. Koli, Effect of the reinforced boron carbide particulate content of AA6061 alloy on formation of the passive film in seawater, *Corros. Sci.* 53 (2011) 2700–2712.
- [8] F. Zhang, J. Brett Wierschke, X. Wang, L. Wang, Nanostructures formation in Al-B<sub>4</sub>C neutron absorbing materials after accelerated irradiation and corrosion tests, *Microsc. Microanal.* 21 (2015) 1159–1160.
- [9] Y.-L. Li, W.-X. Wang, H.-S. Chen, J. Zhou, Q.-C. Wu, Corrosion behavior of B<sub>4</sub>C/6061Al neutron absorber composite in different H<sub>3</sub>BO<sub>3</sub> concentration solutions, *Acta Metal. Sin. (Engl. Lett.)* 29 (2016) 1037–1046.
- [10] H. Ding, L.H. Hihara, Localized corrosion currents and pH profile over B<sub>4</sub>C, SiC, and Al<sub>2</sub>O<sub>3</sub> reinforced 6092 aluminum composites, *J. Electrochem. Soc.* 152 (2005) B161–B167.
- [11] H. Ding, L.H. Hihara, Electrochemical examinations on the corrosion behavior of boron carbide reinforced aluminum-matrix composites, *J. Electrochem. Soc.* 158 (2011) C118–C124.
- [12] H. Ding, L.H. Hihara, Electrochemical behavior of boron carbide and galvanic corrosion of boron carbide reinforced 6092 aluminum composites, *ECS Trans.* 1 (2006) 103–114.
- [13] Y. Zhou, Y. Zan, S. Zheng, X. Shao, Q. Jin, B. Zhang, Q. Wang, B. Xiao, X. Ma, Z. Ma, Thermally stable microstructures and mechanical properties of B<sub>4</sub>C-Al composite with in-situ formed Mg(Al)B<sub>2</sub>, *J. Mater. Sci. Technol.* 35 (2019) 1825–1830.
- [14] X. Pang, Y. Xian, W. Wang, P. Zhang, Tensile properties and strengthening effects of 6061Al/12 wt%B<sub>4</sub>C composites reinforced with nano-Al<sub>2</sub>O<sub>3</sub> particles, *J. Alloys Compd.* 768 (2018) 476–484.
- [15] Y.T. Zhou, Y.N. Zan, X.X. Wei, B. Yang, B. Zhang, S.J. Zheng, X.H. Shao, J.H. Dong, X.L. Ma, B.L. Xiao, Q.Z. Wang, Z.Y. Ma, Corrosion onset associated with the reinforcement and secondary phases in B<sub>4</sub>C-6061Al neutron absorber material in H<sub>3</sub>BO<sub>3</sub> solution, *Corros. Sci.* 153 (2019) 74–84.
- [16] J.R. Davis (Ed.), *Corrosion of Aluminum and Aluminum Alloys*, ASM International, USA, 2000.
- [17] M. Strangwood, C.A. Hipsley, J.J. Lewandowski, Segregation to SiC/Al interfaces in Al based metal matrix composites, *Scripta Metall. Mater.* 24 (1990) 1483–1487.
- [18] K.T. Aust, R.E. Hannerman, P. Niessen, J.H. Westbrook, Solute induced hardening near grain boundaries in zone refined metals, *Acta Metall.* 16 (1968) 291–302.
- [19] J. Man, L. Jing, S.G. Jie, The effects of Cu addition on the microstructure and thermal stability of an Al–Mg–Si alloy, *J. Alloys Compd.* 437 (2007) 146–150.
- [20] M. Fiawoo, X. Gao, L. Bourgeois, N. Parson, X.Q. Zhang, M. Couper, J.F. Nie, Formation of multiple orientation relationships of Q precipitates in Al–Mg–Si–Cu alloys, *Scr. Mater.* 88 (2014) 53–56.
- [21] T. Saito, C.D. Marioara, S.J. Andersen, W. Lefebvre, R. Holmestad, Aberration-corrected HAADF-STEM investigations of precipitate structures in Al–Mg–Si alloys with low Cu additions, *Philos. Mag. Abingdon (Abingdon)* 94 (2013) 520–531.
- [22] S.K. Kairy, P.A. Rometsch, K. Diao, J.F. Nie, C.H.J. Davies, N. Birbilis, Exploring the electrochemistry of 6xxx series aluminium alloys as a function of Si to Mg ratio, Cu content, ageing conditions and microstructure, *Electrochim. Acta* 190 (2016) 92–103.
- [23] G. Svenningsen, M.H. Larsen, J.C. Walmsley, J.H. Nordlien, K. Nisancioglu, Effect of artificial aging on intergranular corrosion of extruded AlMgSi alloy with small Cu content, *Corros. Sci.* 48 (2006) 1528–1543.

- [24] S.K. Kairy, T. Alam, P.A. Rometsch, C.H.J. Davies, R. Banerjee, N. Birbilis, Understanding the origins of intergranular corrosion in copper-containing Al-Mg-Si alloys, *Metall. Mater. Trans. A* 47A (2016) 985–989.
- [25] Y.T. Zhou, Y.N. Zan, S.J. Zheng, Q.Z. Wang, B.L. Xiao, X.L. Ma, Z.Y. Ma, Distribution of the microalloying element Cu in B<sub>4</sub>C-reinforced 6061Al composites, *J. Alloys. Compd.* 728 (2017) 112–117.
- [26] S.J. Pennycook, Structure determination through Z-contrast microscopy, *Adv. Imag. Electron Phys.* 123 (2002) 173–206.
- [27] T.D. Burleigh, E. Ludwiczak, R.A. Petri, Intergranular corrosion of an Aluminum-magnesium-silicon-copper alloy, *Corrosion* 51 (1995) 50–55.
- [28] S.J. Zheng, Y.J. Wang, B. Zhang, Y.L. Zhu, C. Liu, P. Hu, X.L. Ma, Identification of MnCr<sub>2</sub>O<sub>4</sub> nano-octahedron in catalysing pitting corrosion of austenitic stainless steels, *Acta Mater.* 58 (2010) 5070–5085.
- [29] S.R.K. Malladi, F.D. Tichelaar, Q. Xu, M.Y. Wu, H. Terry, J.M.C. Mol, F. Hannour, H.W. Zandbergen, Quasi in-situ analytical TEM to investigate electrochemically induced microstructural changes in alloys: AA2024-T3 as an example, *Corros. Sci.* 69 (2013) 221–225.
- [30] S.K. Kairy, P.A. Rometsch, C.H.J. Davies, N. Birbilis, On the electrochemical and quasi in-situ corrosion response of the Q-phase (Al<sub>x</sub>Cu<sub>y</sub>Mg<sub>z</sub>Si<sub>w</sub>) intermetallic particle in 6xxx series Al-alloys, *Corrosion* 73 (2017) 87–99.
- [31] Z. Fan, Y. Wang, Y. Zhang, T. Qin, X.R. Zhou, G.E. Thompson, T. Pennycook, T. Hashimoto, Grain refining mechanism in the Al/Al–Ti–B system, *Acta Mater.* 84 (2015) 292–304.
- [32] X. Ma, Y. Zhao, X. Zhao, T. Gao, H. Chen, X. Liu, Influence mechanisms of Cu or Fe on the microstructures and tensile properties at 350 °C of network AlN<sub>p</sub> reinforced Al composites, *J. Alloys. Compd.* 740 (2018) 452–460.
- [33] Y. Wang, C.M. Fang, L. Zhou, T. Hashimoto, X. Zhou, Q.M. Ramasse, Z. Fan, Mechanism for Zr poisoning of Al–Ti–B based grain refiners, *Acta Mater.* 164 (2019) 428–439.
- [34] R.G. Buchheit, L.P. Montes, M.A. Martinez, J. Michael, P.F. Hlava, The electrochemical characteristics of bulk-synthesized Al<sub>2</sub>CuMg, *J. Electrochem. Soc.* 146 (1999) 4424–4428.
- [35] R.G. Buchheit, M.A. Martinez, L.P. Montes, Evidence for Cu ion formation by dissolution and dealloying the Al<sub>2</sub>CuMg intermetallic compound in rotating ring-disk collection experiments, *J. Electrochem. Soc.* 147 (2000) 119–124.
- [36] J. Li, W. Sun, B. Hurley, A.A. Luo, R.G. Buchheit, Cu redistribution study during the corrosion of AZ91 using a rotating ring-disk collection experiment, *Corros. Sci.* 112 (2016) 760–764.
- [37] S.L. Pohlman, Corrosion and electrochemical behavior of boron/aluminum composites, *Corrosion* 34 (1978) 157–159.
- [38] A.S. Sharipov, B.I. Loukhovitski, Structure and properties of (AlB<sub>2</sub>)<sub>n</sub> and (MgB<sub>2</sub>)<sub>n</sub> (n = 1, ..., 10) clusters, *Eur. Phys. J. D - At. Mol. Opt. Phys.* 73 (2019) 14.
- [39] A. Serquis, Y.T. Zhu, D.E. Peterson, F.M. Mueller, R.K. Schulze, V.F. Nesterenko, S.S. Indrakanti, Degradation of MgB<sub>2</sub> under ambient environment, *Appl. Phys. Lett.* 80 (2002) 4001–4003.
- [40] H. Zhu, S. Wang, Z. Li, X. Liu, L. Jiang, Degradation behavior of MgB<sub>2</sub> powders in different medium environment, *Mater. Sci. Forum* 650 (2010) 172–177.
- [41] Y.T. Zhou, Y.J. Wang, S.J. Zheng, B. Zhang, X.L. Ma, Strain-induced preferential dissolution at the dislocation emergences in MnS: an atomic scale study, *Philos. Mag. Abingdon (Abingdon)* 95 (2015) 2365–2375.
- [42] X.B. Yang, J.H. Chen, G.H. Zhang, L.P. Huang, T.W. Fan, Y. Ding, X.W. Yu, A transmission electron microscopy study of microscopic causes for localized-corrosion morphology variations in the AA7055 Al alloy, *J. Mater. Sci. Technol.* 34 (2018) 1719–1729.
- [43] B. Zhang, J. Wang, B. Wu, Y.T. Zhou, X.L. Ma, Quasi-in-situ ex-polarized TEM observation on dissolution of MnS inclusions and metastable pitting of austenitic stainless steel, *Corros. Sci.* 100 (2015) 295–305.
- [44] Y.T. Zhou, S.J. Zheng, B. Zhang, X.L. Ma, Atomic scale understanding of the interaction between alloying copper and MnS inclusions in stainless steels in NaCl electrolyte, *Corros. Sci.* 111 (2016) 414–421.
- [45] Y. Zhang, P. Gore, W. Rong, Y. Wu, Y. Yan, R. Zhang, Quasi-in-situ STEM-EDS insight into the role of Ag in the corrosion behaviour of Mg-Gd-Zr alloys, *Corros. Sci.* 136 (2018) 106–118.
- [46] X.H. Shao, Z.Q. Yang, X.L. Ma, Interplay between {10 $\bar{1}$ 2} deformation twins and basal stacking faults enriched with Zn/Y in Mg<sub>97</sub>Zn<sub>1</sub>Y<sub>2</sub> alloy, *Philos. Mag. Lett.* 94 (2014) 150–156.
- [47] J.F. Nie, Y.M. Zhu, J.Z. Liu, X.Y. Fang, Periodic segregation of solute atoms in fully coherent twin boundaries, *Science* 340 (2013) 957–960.
- [48] G. Sha, L. Yao, X. Liao, S.P. Ringer, Z.C. Duan, T.G. Langdon, Segregation of solute elements at grain boundaries in an ultrafine grained Al-Zn-Mg-Cu alloy, *Ultramicroscopy* 111 (2011) 500–555.
- [49] J.M. Rosalie, L. Bourgeois, Silver segregation to  $\theta'$  (Al<sub>2</sub>Cu)-Al interfaces in Al-Cu-Al alloys, *Acta Mater.* 60 (2012) 6033–6041.